

Article

A Phase-Preserving Focusing Technique for TOPS Mode SAR Raw Data Based on Conventional Processing Methods

Adele Fusco , Antonio Pepe , Paolo Berardino, Claudio De Luca , Sabatino Buonanno and Riccardo Lanari * 

IREA—National Research Council of Italy (CNR) via Diocleziano 328, 80124 Napoli, Italy

* Correspondence: lanari.r@irea.cnr.it; Tel.: +39-081-570-5734

Received: 27 February 2019; Accepted: 26 July 2019; Published: 29 July 2019



Abstract: We present a new solution for the phase-preserving focusing of synthetic aperture radar (SAR) raw data acquired through the Terrain Observation with Progressive Scan (TOPS) mode. The proposed algorithm consists of a first interpolation stage of the TOPS raw data, which takes into account the Doppler Centroid frequency variations due to the azimuth antenna steering function, and allows us to unfold the azimuth spectra of the TOPS raw data. Subsequently, the interpolated signals are processed by using conventional phase-preserving SAR focusing methods that exploit frequency domain and spectral analyses algorithms, which are extensively used to efficiently process Stripmap and ScanSAR data. Accordingly, the developed focusing approach is easy to implement. In particular, the presented focusing approach exploits one of the available frequency domain Stripmap processing techniques. The only modification is represented by the inclusion, within the 2D frequency domain focusing step, of a spurious azimuth chirp signal with a properly selected azimuthal rate. This allows us to efficiently carry out the TOPS azimuth focusing through the SPECAN method. Furthermore, an important aspect of this algorithm is the possibility to easily achieve a constant and tunable output azimuth pixel size without any additional computing time; this is a remarkable feature with respect to the full-aperture TOPS-mode algorithms available in the existing literature. Moreover, although tailored on Sentinel-1 (S1) raw data, the proposed algorithm can be easily extended to process data collected through the TOPS mode by different radar sensors. The presented experimental results have been obtained by processing real Sentinel-1 raw data and confirm the effectiveness of the proposed algorithm.

Keywords: TOPS; SAR; Raw data; SAR focusing algorithms; Sentinel-1

1. Introduction

Synthetic Aperture Radar (SAR) is an active microwave sensor which presently plays a fundamental role in the Earth observation scenario [1]. Spaceborne SAR systems typically have the capability to operate with the conventional Stripmap and ScanSAR imaging modes [2–4]. However, the rising demands in having wider swath coverage and/or finer azimuth resolution have led to the development of new advanced imaging modes with improved performance. In particular, the capability to steer the radar antenna beam along the azimuth direction has led to the design of the Spotlight [5,6] and the Terrain Observation by Progressive Scans (TOPS) [7] modes, which are used to achieve enhanced azimuth resolution or wide-swath coverage, respectively. Notably, the TOPS mode is extensively exploited by the Sentinel-1 constellation [8,9], and it is going to be adopted as principal acquisition mode for wide-swath imaging of the TerraSAR-X2 [10] and the Chinese spaceborne SAR missions [11,12]. As with the conventional ScanSAR mode [13], the TOPS imaging mode achieves

wide-swath coverage by switching the antenna beam along range direction from swath to swath (often referred to as sub-swaths), but it is able to achieve better azimuth resolution and to overcome the major ScanSAR drawbacks, i.e., the azimuth-varying signal-to-noise ratio and ambiguity-to-signal ratio as well as the so-called “scalloping” effect, introduced by the antenna steering [7,13]. These effects are undesired and require an appropriate post-processing filtering stage to compensate them in the focused ScanSAR images [14–16].

For what concerns the TOPS mode (at variance with ScanSAR) the antenna beam rotates along azimuth throughout the acquisition from backward to forward, i.e., with the opposite direction to the Spotlight case, and this leads all targets to be illuminated during the acquisition data duration (burst) within a large portion of the azimuth antenna pattern, thus mitigating the above-mentioned SAR image quality degradation effects. A consequence of the TOPS operating mode is that targets located at different azimuth positions are imaged with different squint angles; this implies that the resulting azimuth signals have a larger bandwidth, much greater than the pulse repetition frequency (PRF) used in the Stripmap case. However, because the PRF is maintained the same as the Stripmap mode, the Doppler spectra result aliased. Therefore, the conventional SAR focusing methods implemented in the frequency domain, such as the range-Doppler algorithm (RDA) [17,18], the chirp scaling algorithm (CSA) [19,20], the extended CSA algorithm [21], the Omega-K algorithm [22,23], the 2-D Fast Fourier Transform algorithm [24–27] and the chirp-Z transform algorithm [28,29], are not directly applicable for efficiently focusing TOPS raw data.

In recent years, several imaging methods have been developed to overcome these problems and to process TOPS raw datasets [30–39]. A first group of these algorithms [30,31] relies on the use of sub-apertures. In this case, each burst raw dataset is split into several azimuth blocks (partially overlapped) wherein the PRF is higher than the instantaneous azimuth bandwidth; this allows one to correct the range cell migration (RCM) in each sub-aperture by using one of the above-mentioned Stripmap focusing algorithms based on spectral analyses. However, the major drawback in using sub-apertures is that usually a large number of overlapped small azimuth blocks must be introduced. Accordingly, by also considering the subsequent recombination steps of the sub-apertures and the matched filter used to focus the full-aperture data, the methods based on sub-apertures turn out to be precise but not particularly computationally efficient.

Alternatively, to the sub-aperture methods, full-aperture imaging algorithms have also been proposed [7,30–39]. These techniques are effective but, on the other hand, they require significant modifications with respect to conventional spectral-based Stripmap focusing techniques, and may request the implementation of rather complex additional processing stages. Among these, we remark that an efficient solution is the one presented in [39] which, however, requests a non-trivial modification of the original chirp-Z transform approach to implement the referred moving band chirp-Z transform (MBCZT).

In this paper, we present a new solution for a precise and efficient focusing of TOPS raw data. The proposed algorithm satisfies the phase quality requirements for interferometric applications [40,41], i.e., it belongs to the class of phase-preserving focusing algorithms [42,43]. In particular, the presented approach is based on a first interpolation stage of the range-compressed SAR data, which is accomplished by taking into account the Doppler frequency variation due to the antenna rotation along azimuth direction, and permits to effectively unfold the azimuthal spectra. Subsequently, the range-compressed data are fully focused by using conventional frequency domain and spectral analyses focusing approaches which have been extensively exploited to focus Stripmap and ScanSAR raw data [24–27,44]. Accordingly, the presented TOPS raw data focusing approach is easy to implement. Furthermore, a significant feature of the developed focusing method is the possibility to have a tunable selection of the azimuth pixel dimension of the focused SAR images. This is achieved by artificially introducing, before azimuth compression, a spurious azimuth chirp signal in the 2-D frequency domain, which is subsequently compensated for through the SPECAN approach [44].

The paper is organized as follows. Section 2 addresses the TOPS acquisition geometry and the TOPS signal characteristics. Section 3 describes the proposed TOPS focusing algorithm. Section 4 shows some examples achieved by applying the developed focusing algorithm to Sentinel-1 raw data acquired through the TOPS mode. Discussion and conclusions are finally drawn in Section 5.

2. TOPS Acquisition Mode and System Transfer Function Analysis

The TOPS SAR acquisition mode operates by electronically steering the azimuth beam position from backward to forward, with an antenna angular velocity, namely ω_{rot} , with respect to a virtual rotation center (see Figure 1). Moreover, similarly to the ScanSAR mode [2], the TOPS raw data are acquired in bursts, say of duration T_b , by cyclically changing the antenna beam between adjacent sub-swaths (see Figure 1).

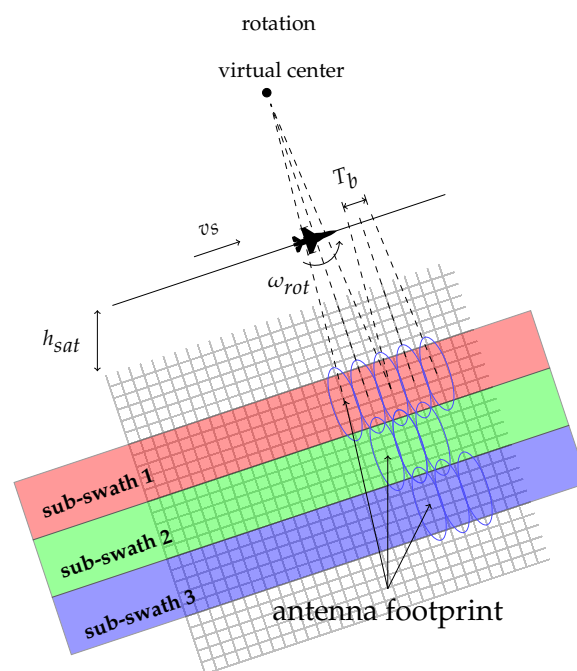


Figure 1. TOPS acquisition mode: the antenna beam has a virtual rotation center located above the platform acquisition track and an angular velocity ω_{rot} . TOPS raw data are acquired in bursts of duration T_b , cyclically switching the antenna beam from swath to swath, referred to as sub-swaths, for wide-area coverage. Note also that v_s and h_{sat} represent the platform velocity and height, respectively.

Figure 2 describes the TOPS SAR geometry for a single burst, where the position of the generic target $P \equiv P(x, r, \theta)$ is defined with respect to a cylindrical coordinates system, whose principal axis x corresponds to the platform flight direction, whereas r represents the range coordinate of the target and θ is the side looking angle.

As evident from Figure 2, due to the antenna azimuth rotation, there is a difference between the platform velocity v_s and the antenna footprint velocity v_f . In particular, we have:

$$v_f \simeq \omega_{rot}(r + r_{rot}) = \omega_{rot}r + v_s. \quad (1)$$

Through simple geometric considerations (see Figure 2), we can derive the illuminated area extension on the ground X_f (see Equation (2)) as follows:

$$X_f \simeq T_b v_f + X \quad (2)$$

where $X = \lambda r/L$ represents the azimuth antenna footprint extension on the ground, being λ the operational wavelength and L the azimuth antenna length. Please note that the ground illuminated area extension X in Equation (2) is typically considered at mid-range. Note also that due to the antenna azimuth rotation, the Doppler Centroid variation with respect to time $DC(t)$ has the following expression:

$$DC(t) = -\frac{2v_s}{\lambda} \sin(\psi_{DC}(t)) \tag{3}$$

where $\psi_{DC}(t) = \omega_{rot}t$, t being the time variable. We further remark that the Doppler Centroid value could also be influenced by a possible squint angle; however, this is neglected in the following analysis.

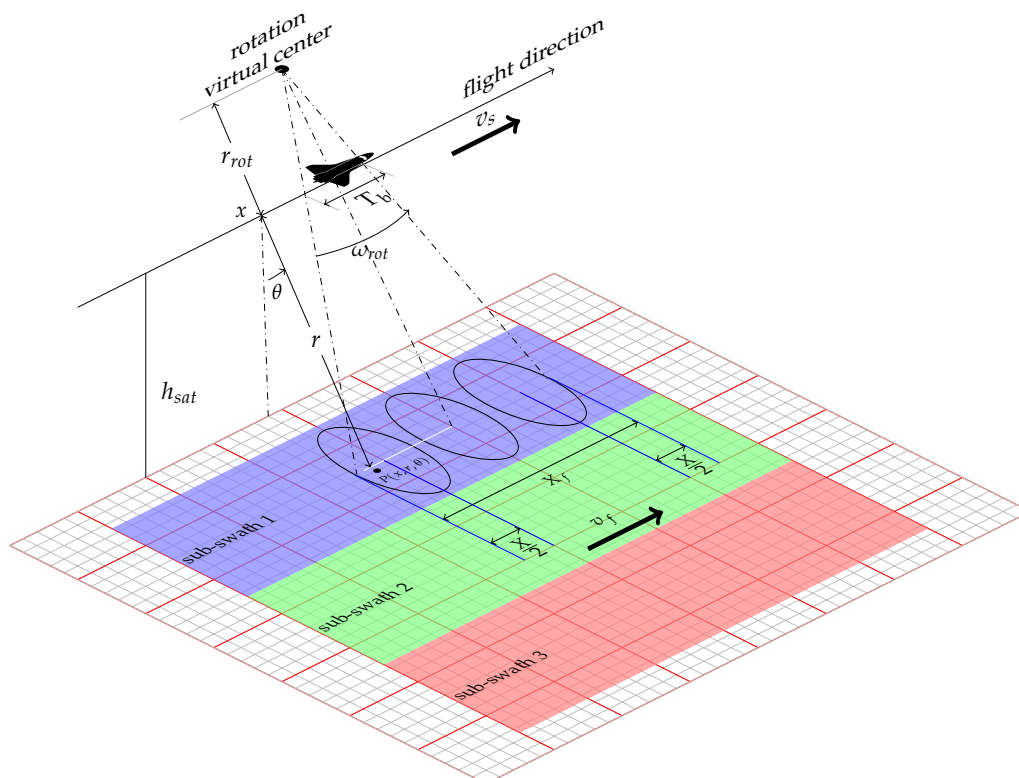


Figure 2. TOPS acquisition geometry for a single burst: $P \equiv P(x, r, \theta)$ represents the location of a generic target, v_s is the sensor velocity, v_f the antenna footprint velocity, ω_{rot} the angular rotation velocity, r_{rot} the distance of the SAR sensor flight track from the virtual rotation center, T_b the acquisition burst time, X_f the illuminated area extension on the ground, X the azimuth antenna footprint.

Let us now concentrate on the derivation of analytical expression of the System Transfer Function (STF) for the TOPS mode, where for the sake of simplicity, inessential amplitude factors are neglected.

We first assume that the SAR system transmits, at time $t_n - \tau/2$, a linearly frequency modulated (FM) chirp, which can be represented by using the complex formalism as follows [3]:

$$s(t - t_n) = \exp[j2\pi f(t - t_n)] \exp[-j\frac{\alpha}{2}(t - t_n)^2] \text{rect}[\frac{t - t_n}{\tau}] \tag{4}$$

where f is the carrier frequency, τ is the pulse duration, and $\alpha = 2\pi\Delta f/\tau$ is the chirp rate, Δf being the transmitted chirp bandwidth. Accordingly, the raw data signal received onboard, related to the point target of radar coordinates $P \equiv P(x, r)$, can be expressed as follows:

$$s_{rec}(t - t_n; x, r) = \exp \left[j2\pi f \left(t - t_n - \frac{2R}{c} \right) \right] \exp \left[-j\frac{\alpha}{2} \left(t - t_n - \frac{2R}{c} \right)^2 \right] \text{rect} \left[\frac{t - t_n - 2R/c}{\tau} \right] W_a^2 \left[\frac{t - t_n - \frac{x}{v_f}}{\frac{X}{v_f}} \right] \text{rect} \left[\frac{t - t_n}{T_b} \right] \text{rect} \left[\frac{x}{X_f} \right] \quad (5)$$

where, as said, we assume that there is no squint angle and $R = \sqrt{r^2 + (v_s(t - t_n) - x)^2} = r + \Delta R$, is the sensor-to-target distance. The received signal includes the two-way azimuth antenna gain $W_a^2[\cdot]$ as well as the effect of the bursting operation due to the TOPS acquisition mode and of the illuminated area extension on the ground.

By neglecting the fast-varying term $\exp [j2\pi f(t - t_n)]$, which is compensated by the heterodyne receiver, and introducing the range $r' = c(t - t_n)/2$ and azimuth $x' = v_s(t - t_n)$ spatial variables, since the *light velocity* is $c = \lambda f$, Equation (5) becomes:

$$s_{rec}(x', r'; x, r) = \exp(-j4\pi r/\lambda) \exp\left(-j4\pi\frac{\Delta R}{\lambda}\right) \exp\left[-j\frac{2\alpha}{c^2}(r' - (r + \Delta R))^2\right] \text{rect}\left[\frac{r' - (r + \Delta R)}{c\tau/2}\right] \text{rect}\left[\frac{\frac{x'}{v_s} - \frac{x}{v_f}}{\frac{X}{v_f}}\right] \text{rect}\left[\frac{\frac{x'}{v_s}}{\frac{X_b}{v_s}}\right] \text{rect}\left[\frac{x}{X_f}\right] \quad (6)$$

where $X_b = v_s \cdot T_b$ is the spatial extension of the flight trajectory during the acquisition burst time T_b . Please note that in Equation (6) the constant phase term $\exp(-j4\pi r/\lambda)$ represents the phase contribution that is explored by the SAR interferometry techniques [3], and the two-way azimuth antenna gain has been approximated with a *rect* function, i.e., $W_a^2[\cdot] = \text{rect}[\cdot]$.

Moreover, it can be easily shown that:

$$\frac{x'}{v_s} - \frac{x}{v_f} = \frac{1}{v_s} \left(x' - \frac{x}{A} \right) \quad (7)$$

where based on Equation (1):

$$A = \frac{v_f}{v_s} = \frac{\omega_{rot}r + v_s}{v_s} = \frac{r + r_{rot}}{r_{rot}} > 1 \quad (8)$$

Accordingly, considering Equations (6)–(8), the TOPS SAR burst impulse response has the following expression:

$$g'(x' - x, r' - r; x, r) = \exp(-j4\pi r/\lambda) \text{rect}\left[\frac{x}{X_f}\right] g(x' - x, r' - r, x, r) \quad (9)$$

where $g(x' - x, r' - r, x, r)$ is:

$$g(x' - x, r' - r, x, r) = \exp\left[-j\frac{2\alpha}{c^2}(r' - (r + \Delta R))^2\right] \text{rect}\left[\frac{r' - (r + \Delta R)}{c\tau/2}\right] \exp\left[-j4\pi\frac{\Delta R}{\lambda}\right] \text{rect}\left[\frac{x' - \frac{x}{A}}{\frac{X}{A}}\right] \text{rect}\left[\frac{x'}{X_b}\right] \quad (10)$$

At this stage, the TOPS transfer function can be obtained by Fourier transforming Equation (10):

$$G(\xi, \eta; x, r) = \int \int dx' dr' g(x' - x, r' - r; x, r) e^{-j2\pi\xi(x' - x)} e^{-j2\pi\eta(r' - r)} \quad (11)$$

where ξ and η denote the azimuth and range spatial frequencies, respectively. Due to the rather large time-bandwidth product of the received signal, the integration in Equation (11) can be carried out via the *stationary phase* method [3,24] thus obtaining, after trivial calculations that:

$$G(\xi, \eta; x, r) = G_{RG}(\eta)G_{TOPS}(\xi, \eta; x, r) \quad (12)$$

where the term:

$$G_{RG}(\eta) \approx \text{rect} \left[\frac{\eta}{2\Delta f/c} \right] \exp \left[-j2\pi \frac{c^2\tau}{8\Delta f} \eta^2 \right] \quad (13)$$

can be straightforwardly compensated during range compression focusing step [2–4] and:

$$G_{TOPS}(\xi, \eta; x, r) \approx \text{rect} \left[\frac{\xi - \frac{2x}{\lambda r} \left(1 - \frac{1}{A}\right)}{\frac{2}{L_e}} \right] \text{rect} \left[\frac{\xi - \frac{2}{\lambda r} x}{\frac{2X_b}{\lambda r}} \right] \exp[-jrk(\xi, \eta)] \quad (14)$$

wherein:

$$L_e = AL > L \quad (15)$$

and

$$k(\xi, \eta) = 2\pi \left[\left(\frac{2}{\lambda} + \eta \right) - \sqrt{\left(\frac{2}{\lambda} + \eta \right)^2 - \xi^2} \right] \approx \frac{\pi\xi^2\lambda}{2} - \frac{\pi\xi^2\eta\lambda^2}{4} \quad (16)$$

We also observe that in Equation (14) the windowing function $\text{rect} \left[\left(\xi - \frac{2}{\lambda r} x \right) / \frac{2X_b}{\lambda r} \right]$ is inessential for the following analysis, because $2X_b/\lambda r > 2/L_e$ and therefore, it has been neglected hereinafter.

We further remark that the term $r k(\xi, \eta)$ in Equation (14) can be written as follows [3,25]:

$$r k(\xi, \eta) = r_0 k(\xi, \eta) + (r - r_0) k(\xi, \eta) \quad (17)$$

Accordingly, Equation (14) can be factorized into a range invariant and range variant phase signal component, as follows:

$$G_{TOPS}(\xi, \eta; x, r) = G_0(\xi, \eta; x, r_0) \cdot G_{\Delta}(\xi, \eta; r - r_0) \quad (18)$$

where considering Equation (16), we have:

$$\begin{aligned} G_0(\xi, \eta; x, r, r_0) &= \text{rect} \left[\frac{\xi - \frac{2x}{\lambda r} \left(1 - \frac{1}{A}\right)}{\frac{2}{L_e}} \right] \exp[-jr_0 k(\xi, \eta)] \simeq \\ &\simeq \text{rect} \left[\frac{\xi - \frac{2x}{\lambda r} \left(1 - \frac{1}{A}\right)}{\frac{2}{L_e}} \right] \exp \left[-jr_0 \left(\frac{\pi\xi^2\lambda}{2} \right) \right] \exp \left[jr_0 \left(\frac{\pi\xi^2\eta\lambda^2}{4} \right) \right] \end{aligned} \quad (19)$$

$$\begin{aligned} G_{\Delta}(\xi, \eta; r - r_0) &= \exp[-j(r - r_0)k(\xi, \eta)] \simeq \\ &\simeq \exp \left[j(r - r_0) \cdot \left(\frac{\pi\xi^2\lambda}{2} - \frac{\pi\xi^2\eta\lambda^2}{4} \right) \right]. \end{aligned} \quad (20)$$

Please note that the approximations presented in Equations (19) and (20) are based on the Taylor expansion in Equation (16) and are rather typical in the SAR Literature. However, they are not essential for the following analysis.

Based on Equations (14), (15) and (19), some considerations are now in order. First, we note that the TOPS azimuth (spatial) spectrum is centered around the Doppler Centroid spatial frequency:

$$\xi'_{Dopp}(x, r) = \frac{2x(1 - 1/A)}{\lambda r} \quad (21)$$

which depends on the angular rotation velocity accounted by A and on the azimuth x and range r position of the target. We further note that L_e , defined in Equation (15), represents a sort of equivalent antenna length for the TOPS mode, which is larger than that of the Stripmap one, thus implying a sort of “shrinking” of the antenna footprint [7].

Accordingly, it is evident that the point-target azimuth TOPS signal spatial bandwidth, which is equal to:

$$B_f = 2/L_e \quad (22)$$

is reduced with respect to the point-target azimuth Stripmap signal spatial bandwidth, which is equal to $2/L$ [1–4], thus leading to an azimuth resolution degradation:

$$\Delta x'_{TOPS} = \frac{L_e}{2} = \frac{AL}{2} > \frac{L}{2}. \quad (23)$$

Moreover, based on from Equations (14) and (21), the total azimuth bandwidth of a single burst B_b can be derived as follows:

$$\begin{aligned} B_b &\simeq \zeta'_{Dopp}\left(\frac{X_f}{2}\right) - \zeta'_{Dopp}\left(-\frac{X_f}{2}\right) + B_f \\ &= \frac{2X_f}{\lambda r}\left(1 - \frac{1}{A}\right) + B_f \end{aligned} \quad (24)$$

as pictorially shown in Figure 3.

As previously stated, we remark that the TOPS raw data are sampled along the azimuth direction by considering a PRF that is consistent with the Stripmap mode bandwidth [2,45], whose spatial expression is PRF/v_s .

Because:

$$\frac{PRF}{v_s} \geq \frac{2}{L} > \frac{2}{L_e} = B_f \quad (25)$$

and

$$\frac{PRF}{v_s} < B_b \quad (26)$$

it turns out that for the TOPS mode the used PRF is greater than the azimuth bandwidth of a single point target (B_f) but it is significantly smaller of the overall bandwidth (B_b), as pictorially shown in Figure 3.

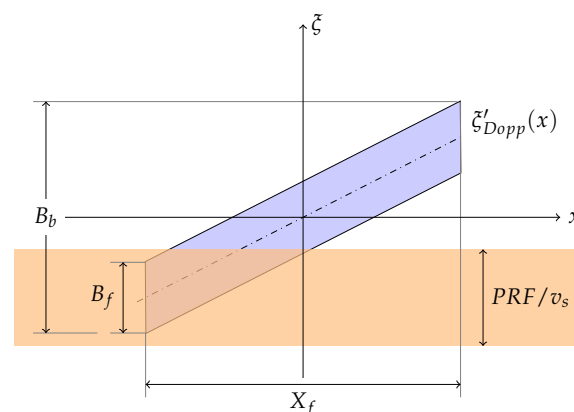


Figure 3. Raw data space/(spatial) frequency representation for the TOPS mode: B_f represents the bandwidth for a single point target, B_b is the overall bandwidth, PRF/v_s is the spatial azimuth pulse repetition frequency, $\zeta'_{Dopp}(x)$ is the Doppler Centroid (spatial) frequency considered here as a function of the azimuth coordinate x .

Accordingly, the TOPS raw data are not correctly sampled at PRF , thus introducing an azimuth spectrum folding. This issue prevents the straightforward application of one of the several computational efficient phase-preserving Stripmap focusing techniques implemented in the frequency domain [17–29]. We propose in the following a simple but effective focusing approach, which relies on the above-mentioned frequency-based Stripmap focusing approaches and on the spectral analysis algorithm referred to as SPECAN method [44].

3. Focusing Algorithm

Let us start this analysis by considering a straightforward implementation, although computationally inefficient, of a TOPS-mode focusing approach. To do this, let us first consider the range-compressed TOPS raw data, for which the $G_{RG}(\eta)$ factor (see Equation (13)) is compensated for in the range frequency domain [2–5]. Subsequently, an azimuthal interpolation is carried out, considering an oversampling factor $N = \lceil B_b/PRF \rceil$, $\lceil \cdot \rceil$ being the ceil operator. Please note that for the TOPS Interferometric Wide-Swath (IWS) mode of the Sentinel-1 A/B sensors N is equal to 5. We further remark that in our implementation the azimuth interpolation is carried out locally by using a sliding window, say of length M (typically equal to 16 samples), to select portions of the raw data samples to be interpolated; in addition, we use Fast Fourier Transform (FFT) codes [46] to achieve high computational efficiency. The implemented procedure is shown in Figure 4.

First of all, for each data block selected by the applied data window, say of length M , the azimuthal frequencies are shifted to zero. This is achieved by multiplying the data with a complex exponential function accounting for the Doppler Centroid value (see Equation (3)) at the center of the selected block. Subsequently, the data can be straightforwardly interpolated through the cascade of an FFT step, a zero-padding block and an inverse FFT [47]. Finally, to restore the phase information of the interpolated signal, we multiply the data with the same complex exponential function used before but with an opposite sign and an increased sampling, accounting for the oversampling factor. Please note that by using a constant Doppler Centroid, it will result in a slight azimuth spectrum aliasing, which is removed by simply using an azimuth bandwidth filter. We further remark that results similar to what we achieve through our interpolation scheme can be obtained by applying the approach based on the spectrum replication and filtering presented in [7]. However, the solution presented in our work is efficient and very simple to implement (see Figure 5). Because the oversampled data have now unfolded azimuth spectra, a conventional Stripmap focusing algorithm [17–29] might straightforwardly be applied. Nonetheless, this strategy is not effective in this case, because to correctly represent each focused burst image, a very large zero padding would be required. Indeed, the number of focused azimuth pixels for each burst image, namely $N_{focused}$, would be much greater than the number of the interpolated raw data azimuth pixels, say N_{interp} , given by :

$$N_{interp} = T_b \cdot PRF_{TOPS} = \frac{X_B}{v_s} N \cdot PRF = \frac{X_B}{\Delta x'} \quad (27)$$

$$N_{focused} = T_f \cdot PRF_{TOPS} = \frac{X_f}{v_s} N \cdot PRF = \frac{X_f}{\Delta x'} \quad (28)$$

thus leading to have

$$N_{focused} = \frac{X_f}{X_B} \cdot N_{interp} \gg N_{interp} \text{ being } X_f \gg X_B \quad (29)$$

where $\Delta x' = v_s/PRF_{TOPS} = v_s/(N \cdot PRF)$ is the output azimuth pixel spacing. To clarify this issue we present in Table 1 typical N_{interp} and $N_{focused}$ values for the sub-swath-1, sub-swath-2 and sub-Swath-3 of the TOPS Interferometric Wide-Swath (IWS) mode of the Sentinel-1 A/B sensors, referred as IW1, IW2, and IW3, respectively.

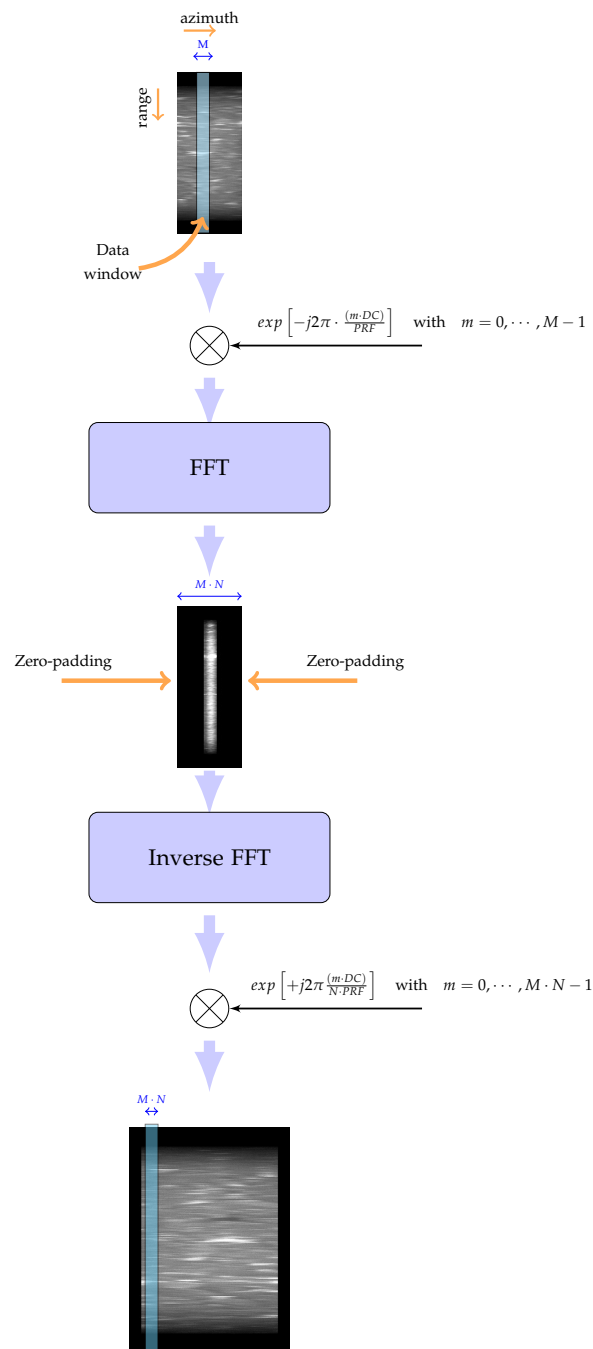


Figure 4. Flow chart of the implemented azimuth interpolation. Please note that PRF is the pulse repetition frequency, DC is the Doppler Centroid, M is the length of the sliding window, and N is the oversampling factor.

Table 1. N_{interp} and $N_{focused}$ values for IW1, IW2, and IW3 sub-swaths of the Sentinel-1 A/B sensors.

Sub-Swaths	N_{interp}	$N_{focused}$
IW1	7021	31919
IW2	7740	28575
IW3	7050	35040

Accordingly, we can clearly argue that the straightforward use of Stripmap focusing algorithms (see Figure 5a) is quite inefficient for processing raw data acquired through the TOPS mode. In the

following, we propose an alternative, efficient approach for an effective exploitation of conventional spectral analysis-based focusing methods.

To do this, we consider the 2-D Fourier transform algorithm [24–27] where, following the previously mentioned azimuth interpolation step, a bulk focusing operation is first performed in 2-D frequency domain. By referring to Equation (19), this operation consists of the compensation of the complex conjugate of the signal $G_0(\xi, \eta; x, r_0)$ shown in Equation (20), within the overall azimuth bandwidth B_b (see Equation (24)).

Moreover, at the same time, we artificially introduce a spurious azimuth chirp signal in the 2-D frequency domain. This is done by multiplying the 2-D spectrum of the compensated bulk-focused TOPS raw signal by the following phase term:

$$Z(\xi) = \exp \left[-j\tilde{r} \left(\frac{\pi\xi^2\lambda}{2} \right) \right] \quad (30)$$

where \tilde{r} is a properly chosen range value, whose selection is clarified in the following. Please note that due to the spurious azimuth chirp signal, the raw data will remain unfocused along the azimuth direction and, therefore the extended azimuth zero padding needed for a conventional Stripmap focusing is not needed in our case. At this stage, following the burst focusing step implemented in 2-D frequency domain, the Stolt mapping operation [48] (which can be implemented in several ways, see [18,19,23,25,28]) is applied, and a 2-D inverse FFT step, is then performed, leading to the signal $\tilde{s}(x', r'; x, r)$. The spurious *defocusing term* (see Equation (30)) is finally compensated by carrying out the convolution, with respect to the azimuth direction, between the signal $\tilde{s}(x' - x; x, r)$ and the relevant chirp signal:

$$\zeta(x'; \tilde{r}) = \exp \left[j2\pi \frac{x'^2}{\lambda\tilde{r}} \right] \quad (31)$$

representing the azimuth inverse Fourier transform of the factor in Equation (30). This convolution operation, expressed as follows:

$$\tilde{s}(x' - x, r'; x, r) \otimes_{az} \zeta(x'; \tilde{r}) \quad (32)$$

is efficiently performed through the SPECAN method [44]. Let us investigate the implementation of this azimuth convolution operation as detailed in [49]. Please note that in this case we refer to a discrete time implementation because it is particularly relevant for our analysis. Hence, we have that for an isolated target of radar coordinates (x, r) , the output signal is:

$$\begin{aligned} \bar{s}(n\Delta x''; x, r) &= \sum_{i=0}^{N_{interp}-1} \tilde{s}(i\Delta x'; x, r) \zeta(n\Delta x'' - i\Delta x') = \\ &= \exp \left[j2\pi \frac{(n\Delta x'')^2}{\lambda\tilde{r}} \right] \sum_{i=0}^{N_{interp}-1} \tilde{s}(i\Delta x'; x, r) \exp \left[j2\pi \frac{(i\Delta x')^2}{\lambda\tilde{r}} \right] \cdot \\ &\quad \cdot \exp \left[-j2\pi \frac{2\Delta x' \Delta x''}{\lambda\tilde{r}} \cdot i \cdot n \right] \quad \text{with } n = 0, \dots, N_{interp} - 1 \end{aligned} \quad (33)$$

where $\Delta x'$ and $\Delta x''$ are the raw data (interpolated) and the focused image azimuth pixel spacings, respectively. Accordingly, the convolution operation is accomplished by the cascade of three stages. First, the signal $\tilde{s}(\cdot)$ is multiplied by the de-ramping term:

$$\exp \left[j2\pi \frac{(i\Delta x')^2}{\lambda\tilde{r}} \right] \quad (34)$$

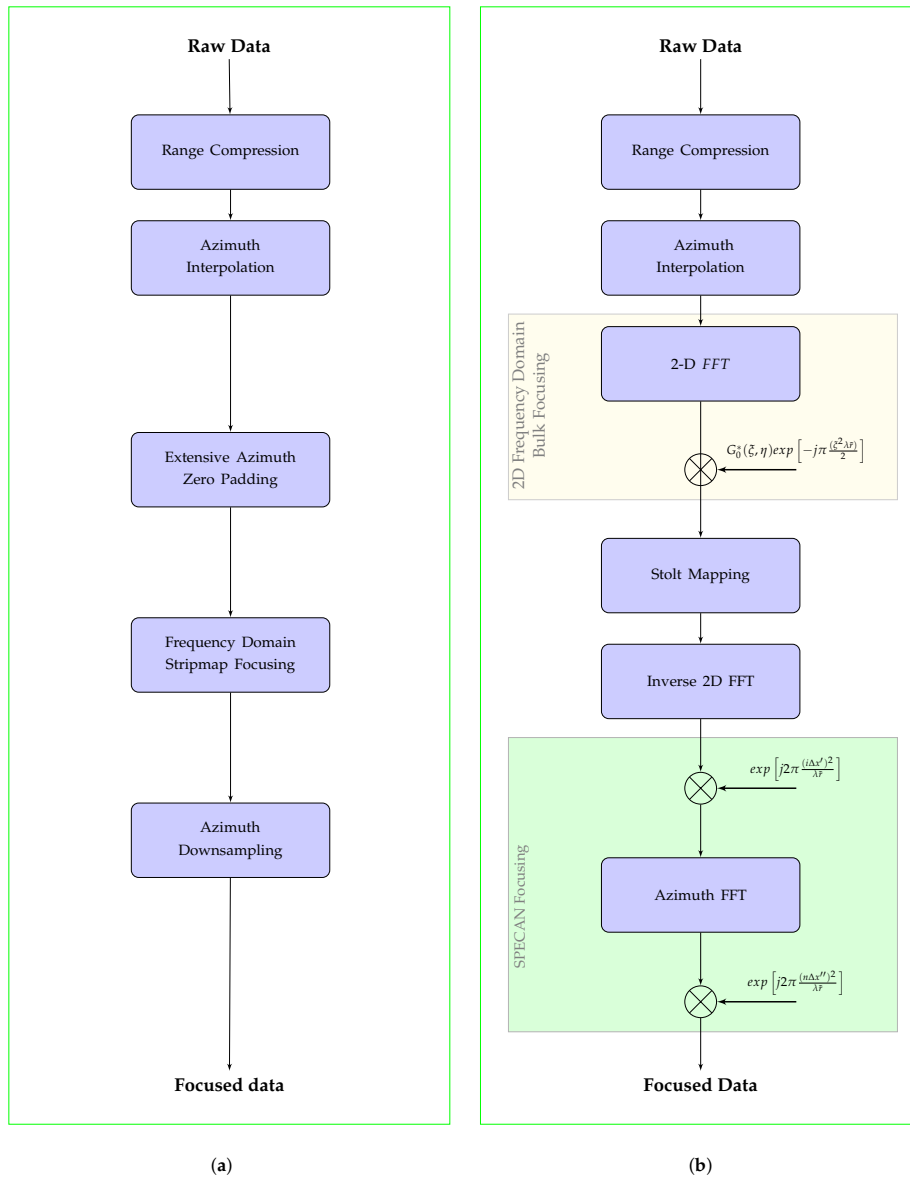


Figure 5. (a) Flow chart of a straightforward Stripmap-based TOPS raw data focusing algorithm; (b) Flow chart of the proposed TOPS raw data focusing algorithm.

Second, a *DFT* operation is performed through the computationally efficient *FFT* algorithm [46]; to this aim the range value \tilde{r} has to be chosen as follows:

$$2 \frac{\Delta x' \Delta x''}{\lambda \tilde{r}} = \frac{1}{N_{interp}}. \quad (35)$$

Finally, the achieved result is multiplied by the residual phase $\exp \left[j2\pi (n\Delta x'')^2 / \lambda \tilde{r} \right]$ and the focused burst is obtained.

The above analysis shows that through an appropriate selection of the \tilde{r} factor of an artificially introduced spurious azimuth chirp, we may exploit a conventional Stripmap algorithm followed by a SPECAN operation, leading out to focused TOPS image bursts without any extensive zero padding of the TOPS raw data. We further remark that the achieved algorithm simplicity justifies some efficiency loss due to the implemented raw data oversampling step (see Figure 4). As further remark, we underline that the burst-focused SAR image is usually under-sampled by a factor, say N_{under} , to reduce the amount of data to be handled.

Figure 5b synthesizes the block diagram of the algorithm presented in this section. Additionally, Figure 6 shows the effect of each processing step of the presented algorithm on the data, starting from raw up to focused data. We further remark that the final step of the presented has some similarities with the MBCZT operation proposed in [39]. Moreover, we also remark that the proposed approach has the interesting degree of freedom to allow the selection of the output pixel spacing $\Delta x''$, see Equation (35). This is an interesting feature which characterizes the presented approach with respect to most of the full-aperture TOPS-mode imaging algorithms available in the existing literature [30–39]. We finally underline that the application of a Stripmap processing approach different from that considered here (see [24–27]) would have no impact on the validity of the proposed TOPS raw data focusing algorithm.

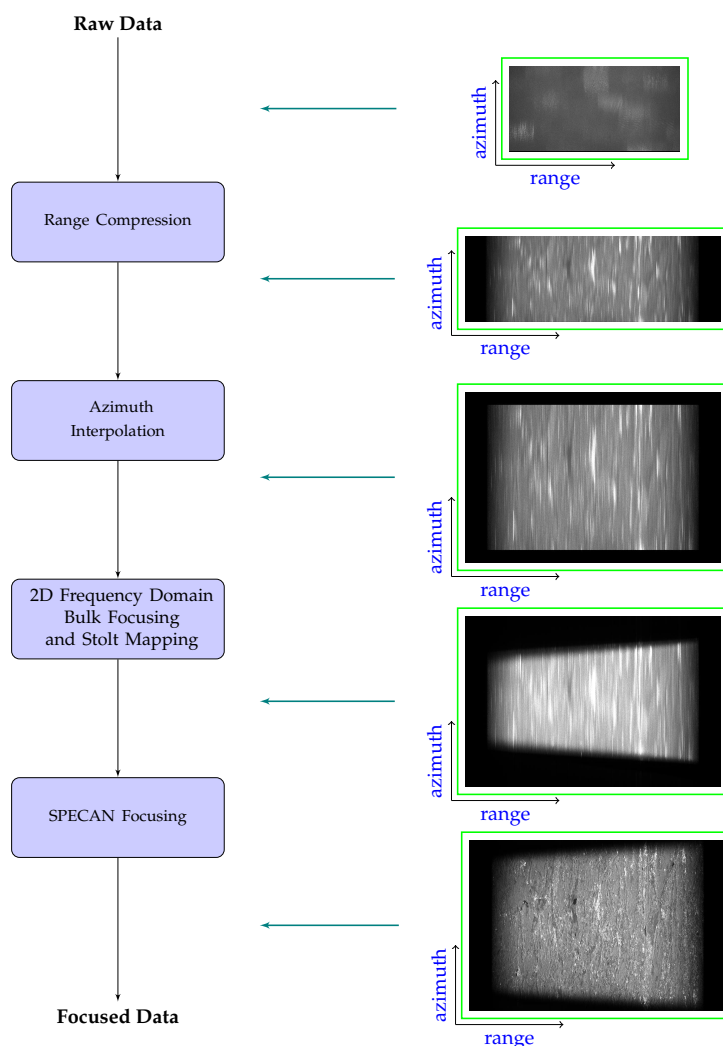


Figure 6. Flow chart of the proposed TOPS raw data focusing algorithm (see Figure 5b), showing the effect of each processing step on the data, starting from raw up to focused data. Please note that the extra zeros shown in the central panel of the Figure have been added only to have an azimuth dimension as power of 2 to efficiently perform the FFT operations.

4. Experimental Results from Sentinel-1 IWS Data

This section illustrates the achieved results obtained by applying the presented focusing algorithm, shown in Figures 5b and 6, to Sentinel-1 raw data acquired through the TOPS IWS mode, with the main parameters summarized in Table 2.

Table 2. Sentinel-1A/B raw data parameters

Parameter	Swath	Value	Unit
Wavelength		0.055465756	m
Azimuth antenna size		12.300000	m
Number of sub-swaths		3	
Sampling Frequency	IW1	64,345,238	Hz
	IW2	54,595,960	Hz
	IW3	46,918,403	Hz
Range pixel spacing	IW1	2.3295620	m
	IW2	2.74555257	m
	IW3	3.194827944	m
Pulse Repetition Frequency	IW1	1717.1290	Hz
	IW2	1451.6271	Hz
	IW3	1685.8173	Hz
Azimuth pixel spacing	IW1	4.1779080	m
	IW2	4.9388437	m
	IW3	4.2459002	m
Angular Steering rate	IW1	1.5903688	degrees/s
	IW2	0.97986332	degrees/s
	IW3	1.3974408	degrees/s

In particular, the investigated raw data include the Deutsche Zentrum für Luft-und Raumfahrt (DLR) calibration site, located in Southern Germany, where some corner reflectors are installed (see Figure 7).

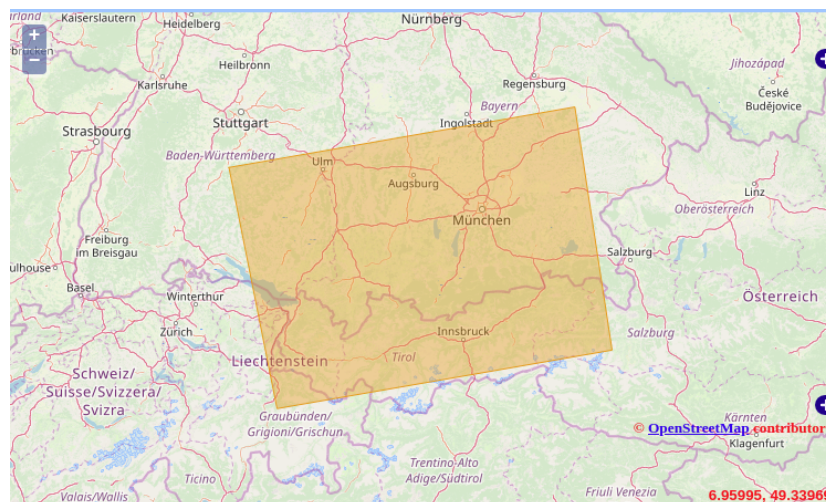


Figure 7. Sentinel 1 Interferometric Wide-Swath TOPS Mode imaged area: the yellow rectangle represents the investigated zone located in Southern Germany.

This area has already been used for geometric, radiometric, and polarimetric calibration of several spaceborne SAR missions such as TerraSAR-X, TanDEM-X, S-1A and S-1B [50]. For the current study, two corner reflectors were used as reference targets.

Figure 8 shows the sequence of the focused TOPS burst images of Sentinel-1B raw dataset acquired on 1 January 2019 over the investigated area. The covered zone extended for about 250 Km × 200 Km. Please note that no antenna pattern correction has been applied. This image was used to analyze the response of the sensed corner reflectors to evaluate the developed focusing algorithm performance in term of spatial resolution and Peak Sidelobe Ratio (PSLR), as it will be described in the following.

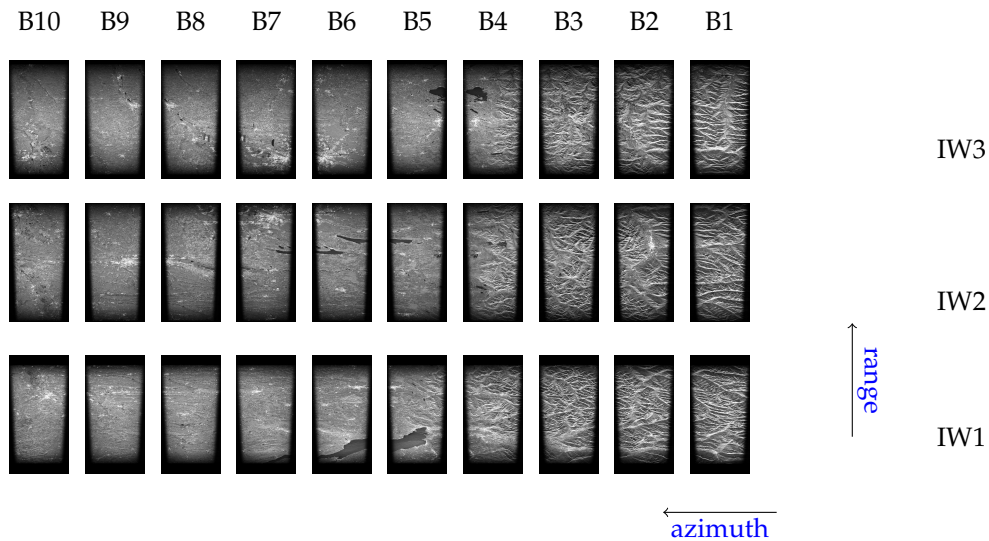


Figure 8. TOPS image focusing result: burst images sequence of the Sentinel-1B raw dataset acquired on 1 January 2019 on the area of interest.

In Table 3, the parameters relevant to the focused burst images are summarized. We highlight here that the output values of the implemented processor have been selected in order to be consistent with those of the image focused through the ESA processor generating the products available on the SciHub catalog [51]; to do this, an under-sampling factor $N_{under} = 4$ has been used. On the other hand we remark that the azimuthal pixel spacing obtained through the developed focusing approach can be selected, depending on the user needs, by simply changing the \tilde{r} value in Equation (35).

Table 3. Sentinel-1A/B parameters of the focused burst images sequence.

Parameter	Swath	Value	Unit
Sampling Frequency	all	64345238	Hz
Range Pixel Spacing	all	2.3295620	m
Pulse Repetition Frequency	all	486.48631	Hz
Azimuth Pixel Spacing	all	14.713116	m

Figure 9 shows a one dimensional cut of the *Impulse Response Function* (IRF) of an ideal point target, along the range or azimuth direction and two quality parameters: the spatial resolution and the PSLR, respectively [2–4].

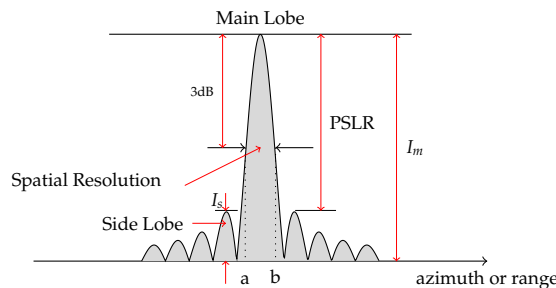


Figure 9. Impulse Response function and related parameters.

Figure 10 shows the focused image relevant to burst 8 of the sub-swath 1, wherein the investigated corner reflectors have been highlighted.

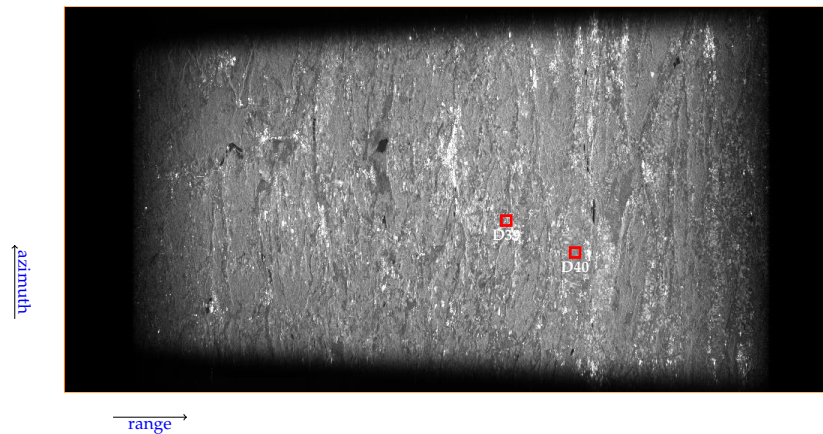


Figure 10. Focused image of burst 8 relevant to sub-swath 1: the position of two corner reflectors, referred to as D39 and D40 (see [50]), has been highlighted by the red squares.

In Figure 11 the IRF central cross sections, along the range and azimuth direction, are displayed for the detected corner reflectors.

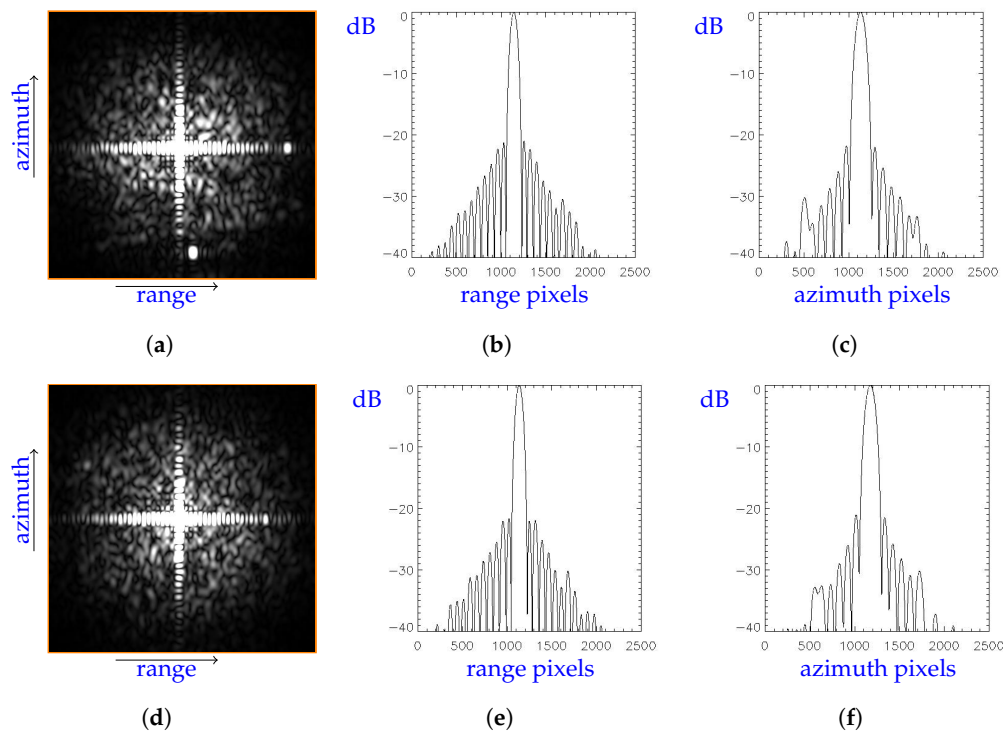


Figure 11. Corner reflectors within the burst 8 of sub-swath 1: (a) image, (b) IRF central cross section along range direction expressed in dB, (c) IRF central cross section along azimuth direction expressed in dB, for the corner reflector D39. (d) image, (e) IRF central cross section along range direction expressed in dB, (f) IRF central cross section along azimuth direction expressed in dB, for the corner reflector D40.

Quantitative results of the image quality analysis for the proposed focusing processing are listed in Table 4, where quality parameters for two corner reflectors within the focused burst 8 of sub-swath 1 have been considered. In particular, ρ_{rg} and $\hat{\rho}_{rg}$ are the nominal and estimated range spatial resolutions, respectively, and ρ_{az} and $\hat{\rho}_{az}$ are the corresponding values along the azimuth. Moreover, the nominal and estimated PLSR ($PSLR$ and \widehat{PLSR} , respectively) along range and azimuth has also presented.

Analogously, quantitative results of the image quality analysis on the corresponding product available through the ESA Schiub archive are listed in Table 5.

Table 4. Quality parameters for the corner reflectors focused through the presented algorithm within burst 8 of sub-swath 1: the nominal and estimated spatial resolutions along range (ρ_{rg} and $\hat{\rho}_{rg}$, respectively), along azimuth (ρ_{az} and $\hat{\rho}_{az}$, respectively), the nominal and estimated PLSR ($PSLR$ and \widehat{PSLR} , respectively) along range and azimuth are presented.

CRs	ρ_{rg} (Nominal) [m]	$\hat{\rho}_{rg}$ [m]	ρ_{az} (Nominal) [m]	$\hat{\rho}_{az}$ [m]	PSLR (Nominal) [dB]	\widehat{PSLR} (Range) [dB]	\widehat{PSLR} (Azimuth) [dB]
D39	2.66	2.66	23.22	23.27	−21.21	−21.13	−21.92
D40	2.66	2.66	23.22	23.5	−21.21	−21.87	−21.35

Table 5. Quality parameters for the corner reflectors focused through the ESA processor within burst 8 of sub-swath 1: the nominal and estimated spatial resolutions along range (ρ_{rg} and $\hat{\rho}_{rg}$, respectively), along azimuth (ρ_{az} and $\hat{\rho}_{az}$, respectively), the nominal and estimated PLSR ($PSLR$ and \widehat{PSLR} , respectively) along range and azimuth are presented.

CRs	ρ_{rg} (Nominal) [m]	$\hat{\rho}_{rg}$ [m]	ρ_{az} (Nominal) [m]	$\hat{\rho}_{az}$ [m]	PSLR (Nominal) [dB]	\widehat{PSLR} (Range) [dB]	\widehat{PSLR} (Azimuth) [dB]
D39	2.66	2.66	23.22	24.88	−21.21	−21.16	−22.68
D40	2.66	2.66	23.22	24.65	−21.21	−21.82	−21.85

By comparing the achieved parameters for the presented focusing method (see Table 4) and the ESA products (see Table 5) with respect to the expected (nominal) values we find out a very good correspondence. Moreover, a slightly better azimuth resolution is achieved by the presented approach. Accordingly, we can promptly conclude that the proposed method has a very good performance. Please note also that to carry out the presented comparison an Hamming-0.75 weighting function has been applied to the burst image focused with the proposed method, in order to be consistent with the characteristics of the ESA images.

As final result, in order to verify the phase-preserving capability of the presented focusing method, we show in Figure 12 a burst interferogram and the corresponding coherence, obtained by processing, through the presented approach, an S1B raw dataset acquired on August 23rd 2018 and an S1A raw dataset acquired six days later; also in this case the considered burst is relevant to the DLR calibration site shown in Figure 10. The interferometric results presented in Figure 12, wherein the flat Earth phase component has been removed [41], fully confirm the phase-preserving capability of our approach.

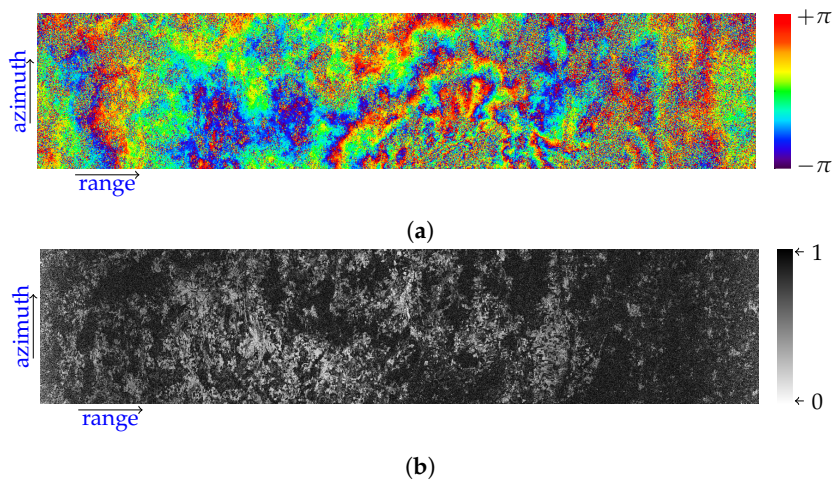


Figure 12. Burst interferogram (a) and the corresponding coherence (b) computed from the pair, focused through the presented approach, relevant to the S1B raw dataset acquired on August 23rd 2018 and the S1A raw dataset acquired six days later, over the DLR calibration site, shown in Figure 10

5. Conclusions and Further Developments

In this work, an effective algorithm to focus SAR raw data acquired through the TOPS mode has been presented.

The proposed method allows the exploitation of conventional frequency domain and spectral analyses techniques, originally developed for processing Stripmap and ScanSAR raw data. In particular, although the presented technique is not dependent on the chosen frequency domain Stripmap processing approach, we consider the algorithm presented in [24–27]. In this case, the only modification with respect to the original technique is the inclusion, within the 2-D frequency domain focusing step, of a spurious azimuth chirp signal with a properly chosen constant rate. This allows us to avoid the extended azimuth zero padding, which would be needed to focus the raw data through a straightforward Stripmap processing approach, and to exploit the high efficient SPECAN method [44] for the final azimuthal focusing of the TOPS raw data. Moreover, our approach also permits to easily achieve a constant and tunable output azimuth pixel size. This is a remarkable feature of the presented approach, with respect to the full-aperture TOPS-mode algorithms available in the existing literature.

Accordingly, the presented TOPS raw data focusing scheme is simple to be implemented and rather efficient, being based on FFTs and matrix multiplications, only. The experimental results, which have been carried out on a real Sentinel-1 SAR datasets relevant to the calibration site of DLR, confirmed the validity of the proposed focusing technique. In particular, the performance of the presented TOPS raw data focusing algorithm have been successfully tested by calculating some quality parameters, e.g., the spatial resolution and the PSLR of the SAR image impulsive response, in correspondence with available corner reflectors in the selected scene. Moreover, the phase-preserving capability of our approach has been demonstrated through the generation of interferometric products relevant to considered test site.

We further remark that the developed phase-preserving focusing algorithm can be effectively integrated in SAR processing toolboxes. Besides, the adopted focusing scheme is suitable for an easy implementation in a parallel computing environment, thus making profit from High-Performance Computing (HPC) architectures. Therefore, future actions will include the optimization of the different steps of the focusing processing based on their efficient implementation by using multi-core and GPUs parallelization [52–54]. To this end, the processing parts that can be parallelized both in terms of processes (multi-core parallelization for multiple bursts focusing processes) and in terms of data (parallelization within a single burst focusing process by using GPUs) will be identified. Accordingly, new modules (GPU kernels) making an efficient use of both cores and memory available on GPUs for parallel data processing, and modules that will exploit multithreading on the host machine (CPU), will be developed.

Author Contributions: A.F. and R.L. developed the proposed TOPS raw data focusing algorithm. P.B. analyzed the focused SAR images for the estimation of synthetic parameters of SAR impulsive response. C.D.L. and S.B. contributed to the realization of the experimental results. A.P. revised the literature and contributed to the algorithm development.

Funding: This work was carried out thanks to the Italian national research program RITMARE financed in 2012–2016 by the Italian Ministero dell' Istruzione, dell' Università e della Ricerca, the projects NextGEOSS and EPOS under the EU Horizon 2020 Framework Programme, the agreement between IREA and the Italian Dipartimento della Protezione Civile, Presidenza del Consiglio dei Ministri, signed on December 2016, the Project of National Interest (PRIN) URBAN-GEO BIG DATA, funded by the Ministero dell' Istruzione, dell' Università e della Ricerca, grant number 20159CNLW8.

Acknowledgments: The authors would thank Nuno Miranda, Michele Manunta, Francesco Casu and, particularly, Riccardo Piantanida for their support given in developing this work. The authors are also grateful to Simone Guarino, Ferdinando Parisi and Maria Consiglia Rasulo of the Istituto per il Rilevamento Elettromagnetico dell' Ambiente, Italian National Research Council, for their continuous technical assistance.

Conflicts of Interest: The authors declare no conflict of interest.

Abbreviations

The following abbreviations are used in this manuscript:

CSA	Chirp Scaling Algorithm
DC	Doppler Centroid
DLR	Deutsches Zentrum für Luft- und Raumfahrt
HPC	High-Performance Computing
IRF	Impulse Response Function
IWS	Interferometric Wide-Swath
PRF	Pulse Repetition Frequency
PSLR	Peak Side Lobe Ratio
RCM	Range Cell Migration
RDA	Range-Doppler Algorithm
SAR	Synthetic Aperture RADAR
TOPS	Terrain Observation by Progressive Scans

References

1. Moreira, A.; Prats-Iraola, P.; Younis, M.; Krieger, G.; Hajnsek, I.; Papathanassiou, K.P. A tutorial on synthetic aperture radar. *IEEE Geosci. Remote Sens. Mag.* **2013**, *1*, 6–43. [[CrossRef](#)]
2. Curlander, J.C.; McDonough, R.N. *Synthetic Aperture Radar—Systems And Signal Processing*; John Wiley & Sons, Inc.: Hoboken, NJ, USA, 1991.
3. Franceschetti, G.; Lanari, R. *Synthetic Aperture Radar Processing*; Electronic Engineering Systems, Taylor & Francis: Boca Raton, FL, USA, 1999.
4. Cumming, I.; Wong, F. *Digital Processing of Synthetic Aperture Radar Data: Algorithms and Implementation*; Number v. 1 in Artech House remote sensing library, Artech House: Norwood, MA, USA, 2005.
5. Carrara, W.; Goodman, R.; Majewski, R. *Spotlight Synthetic Aperture Radar: Signal Processing Algorithms*; Artech House signal processing library, Artech House: Norwood, MA, USA, 1995.
6. Baker, D.P.B.C.J. High resolution processing of hybrid strip-map/spotlight mode SAR. *IET J. Mag.* **1996**, *143*, 366–374.
7. De Zan, F.; Guarnieri, A.M. TOPSAR: Terrain Observation by Progressive Scans. *IEEE Trans. Geosci. Remote Sens.* **2006**, *44*, 2352–2360. [[CrossRef](#)]
8. Torres, R.; Snoeij, P.; Geudtner, D.; Bibby, D.; Davidson, M.; Attema, E.; Potin, P.; Rommen, B.; Floury, N.; Brown, M.; et al. GMES Sentinel-1 mission. *Remote Sens. Environ.* **2012**, *120*, 9–24. [[CrossRef](#)]
9. Geudtner, D.; Torres, R.; Snoeij, P.; Davidson, M.; Rommen, B. Sentinel-1 System capabilities and applications. In Proceedings of the 2014 IEEE Geoscience and Remote Sensing Symposium, Quebec City, QC, Canada, 13–18 July 2014; pp. 1457–1460. [[CrossRef](#)]
10. Janoth, J.; Gantert, S.; Schrage, T.; Kaptein, A. Terrasar next generation—Mission capabilities. In Proceedings of the 2013 IEEE International Geoscience and Remote Sensing Symposium—IGARSS, Melbourne, VIC, Australia, 21–26 July 2013; pp. 2297–2300. [[CrossRef](#)]
11. Xu, W.; Huang, P.; Deng, Y.K. MIMO-TOPS mode for high-resolution ultra-wide-swath full polarimetric imaging. *Progress Electromagn. Res.* **2011**, *121*, 19–37. [[CrossRef](#)]
12. Deng, Y.; Huang, M. Tri-band Multi-Polarity Airborne SAR System. In Proceedings of the 8th European Conference on Synthetic Aperture Radar, Aachen, Germany, 7–10 June 2010; pp. 1–3.
13. Tomiyasu, K. Conceptual Performance of a Satellite Borne, Wide Swath Synthetic Aperture Radar. *IEEE Trans. Geosci. Remote Sens.* **1981**, *GE-19*, 108–116. [[CrossRef](#)]
14. Bamler, R. Optimum look weighting for burst-mode and ScanSAR processing. *IEEE Trans. Geosci. Remote Sens.* **1995**, *33*, 722–725. [[CrossRef](#)]
15. Shimada, M. A New Method for Correcting ScanSAR Scalloping Using Forests and Inter-SCAN Banding Employing Dynamic Filtering. *IEEE Trans. Geosci. Remote Sens.* **2009**, *47*, 3933–3942. [[CrossRef](#)]
16. Romeiser, R.; Horstmann, J.; Graber, H. A new scalloping filter algorithm for scansar images. In Proceedings of the 2010 IEEE International Geoscience and Remote Sensing Symposium, Honolulu, HI, USA, 25–30 July 2010; pp. 4079–4082. [[CrossRef](#)]

17. Cumming, I.; Bennett, J. Digital processing of Seasat SAR data. In Proceedings of the IEEE International Conference on Acoustics, Speech, and Signal Processing (ICASSP'79), Washington, DC, USA, 2–4 April 1979; Volume 4, pp. 710–718. [[CrossRef](#)]
18. Bamler, R. A comparison of range-Doppler and wavenumber domain SAR focusing algorithms. *IEEE Trans. Geosci. Remote Sens.* **1992**, *30*, 706–713. [[CrossRef](#)]
19. Raney, R.K.; Runge, H.; Bamler, R.; Cumming, I.G.; Wong, F.H. Precision SAR processing using chirp scaling. *IEEE Trans. Geosci. Remote Sens.* **1994**, *32*, 786–799. [[CrossRef](#)]
20. Hughes, W.; Gault, K.; Princz, G.J. A comparison of the Range-Doppler and Chirp Scaling algorithms with reference to RADARSAT. In Proceedings of the 1996 International Geoscience and Remote Sensing Symposium (IGARSS'96), Lincoln, NE, USA, 31–31 May 1996; Volume 2, pp. 1221–1223. [[CrossRef](#)]
21. Moreira, A.; Mittermayer, J.; Scheiber, R. Extended chirp scaling algorithm for air- and spaceborne SAR data processing in stripmap and ScanSAR imaging modes. *IEEE Trans. Geosci. Remote Sens.* **1996**, *34*, 1123–1136. [[CrossRef](#)]
22. Rocca, F.; Cafforio, C.; Prati, C. Synthetic Aperture Radar for wave application techniques. *Geophys. Prospect.* **1989**, *37*, 809–830. [[CrossRef](#)]
23. Cafforio, C.; Prati, C.; Rocca, F. SAR data focusing using seismic migration techniques. *IEEE Trans. Aerosp. Electron. Syst.* **1991**, *27*, 194–207. [[CrossRef](#)]
24. Franceschetti, G.; Schirinzi, G. A SAR processor based on two-dimensional FFT codes. *IEEE Trans. Aerosp. Electron. Syst.* **1990**, *26*, 356–366. [[CrossRef](#)]
25. Franceschetti, G.; Lanari, R.; Pascazio, V.; Schirinzi, G. WASAR: a wide-angle SAR processor. *IEE Proc. F Radar Signal Process.* **1992**, *139*, 107–114. [[CrossRef](#)]
26. Franceschetti, G.; Lanari, R.; Marzouk, E.S. Efficient and high precision space-variant processing of SAR data. *IEEE Trans. Aerosp. Electron. Syst.* **1995**, *31*, 227–237. [[CrossRef](#)]
27. Franceschetti, G.; Lanari, R.; Marzouk, E.S. A new two-dimensional squint mode SAR processor. *IEEE Trans. Aerosp. Electron. Syst.* **1996**, *32*, 854–863. [[CrossRef](#)]
28. Lanari, R. A new method for the compensation of the SAR range cell migration based on the chirp z-transform. *IEEE Trans. Geosci. Remote Sens.* **1995**, *33*, 1296–1299. [[CrossRef](#)]
29. Lanari, R.; Fornaro, G. A short discussion on the exact compensation of the SAR range-dependent range cell migration effect. *IEEE Trans. Geosci. Remote Sens.* **1997**, *35*, 1446–1452. [[CrossRef](#)]
30. Mittermayer, J.; Lord, R.; Borner, E. Sliding spotlight SAR processing for TerraSAR-X using a new formulation of the extended chirp scaling algorithm. In Proceedings of the 2003 IEEE International Geoscience and Remote Sensing Symposium. Proceedings (IEEE Cat. No.03CH37477), Toulouse, France, 21–25 July 2003; Volume 3, pp. 1462–1464. [[CrossRef](#)]
31. Prats, P.; Scheiber, R.; Mittermayer, J.; Meta, A.; Moreira, A. Processing of Sliding Spotlight and TOPS SAR Data Using Baseband Azimuth Scaling. *IEEE Trans. Geosci. Remote Sens.* **2010**, *48*, 770–780. [[CrossRef](#)]
32. Xu, W.; Huang, P.; Deng, Y. TOPSAR data focusing based on azimuth scaling preprocessing. *Adv. Space Res.* **2011**, *48*, 270–277. [[CrossRef](#)]
33. Huang, P.; Xu, W. An efficient imaging approach for TOPS SAR data focusing based on scaled fourier transform. *Progress Electromagn. Res.* **2013**, *47*, 297–313. [[CrossRef](#)]
34. Sun, G.; Xing, M.; Wang, Y.; Wu, Y.; Wu, Y.; Bao, Z. Sliding Spotlight and TOPS SAR Data Processing Without Subaperture. *IEEE Geosci. Remote Sens. Lett.* **2011**, *8*, 1036–1040. [[CrossRef](#)]
35. Xu, W.; Huang, P.; Deng, Y.; Sun, J.; Shang, X. An Efficient Approach With Scaling Factors for TOPS-Mode SAR Data Focusing. *IEEE Geosci. Remote Sens. Lett.* **2011**, *8*, 929–933. [[CrossRef](#)]
36. Xu, W.; Huang, P.; Wang, R.; Deng, Y.; Lu, Y. TOPS-Mode Raw Data Processing Using Chirp Scaling Algorithm. *IEEE J. Sel. Top. Appl. Earth Obs. Remote Sens.* **2014**, *7*, 235–246. [[CrossRef](#)]
37. Yang, W.; Chen, J.; Zeng, H.C.; Wang, P.B.; Liu, W. A Wide-Swath Spaceborne TOPS SAR Image Formation Algorithm Based on Chirp Scaling and Chirp-Z Transform. *Sensors* **2016**, *16*, 2095. [[CrossRef](#)] [[PubMed](#)]
38. Yang, W.; Chen, J.; Liu, W.; Wang, P.; Li, C. A Modified Three-Step Algorithm for TOPS and Sliding Spotlight SAR Data Processing. *IEEE Trans. Geosci. Remote Sens.* **2017**, *55*, 6910–6921. [[CrossRef](#)]
39. Engen, G.; Larsen, Y. Efficient Full Aperture Processing of TOPS Mode Data Using the Moving Band Chirp Z-Transform. *IEEE Trans. Geosci. Remote Sens.* **2011**, *49*, 3688–3693. [[CrossRef](#)]
40. Massonnet, D.; Feigl, K.L. Radar interferometry and its application to changes in the Earth's surface. *Rev. Geophys.* **1998**, *36*, 441–500. [[CrossRef](#)]

41. Rosen, P.A.; Hensley, S.; Joughin, I.R.; Li, F.K.; Madsen, S.N.; Rodriguez, E.; Goldstein, R.M. Synthetic aperture radar interferometry. *Proc. IEEE* **2000**, *88*, 333–382. [[CrossRef](#)]
42. Bamler, R.; Schättler, B. *Phase-Preservation in SAR Processing: Definition, Requirements and Tests*; DLR Tech, Note Ver 1.0; DLR Publisher: Oberpfaffenhofen, Germany, 1995.
43. ESA. *RADAR and SAR Glossary*; 2019. Available online: <https://earth.esa.int/handbooks/asar/CNTR5-2.html> (accessed on 28 July 2019).
44. Sack, M.; Ito, M.R.; Cumming, I.G. Application of efficient linear FM matched filtering algorithms to synthetic aperture radar processing. *IEE Proc. F (Commun. Radar Signal Process.)* **1985**, *132*, 45–57. [[CrossRef](#)]
45. Piantanida, R.; Hajduch, G.; Poullaouec, J. *Sentinel-1 Level 1 Detailed Algorithm Definition*; Technical Report; MDA: Chicago, IL, USA, 2017.
46. Cooley, J.W.; Tukey, J.W. An algorithm for the machine calculation of complex Fourier series. *Math. Comput.* **1965**, *19*, 297–301. [[CrossRef](#)]
47. Lyons, R.G. *Understanding Digital Signal Processing*, 2nd ed.; Prentice Hall PTR: Upper Saddle River, NJ, USA, 2004.
48. Stolt, R.H. Migration by Fourier Transform. *Geophysics* **1978**, *43*, 23–48. [[CrossRef](#)]
49. Lanari, R.; Hensley, S.; Rosen, P.A. Chirp z-transform based SPECAN approach for phase-preserving ScanSAR image generation. *IEE Proc. -Radar Sonar Navig.* **1998**, *145*, 254–261.:19982218. [[CrossRef](#)]
50. Reimann, J.; Schwerdt, M.; Schmidt, K.; Ramon, N.T.; Castellanos, G.A.; Döring, B.; Rudolf, D.; Raab, S.; Antony, J.M.W.; Zink, M. The DLR SAR calibration center. In Proceedings of the 2015 IEEE 5th Asia-Pacific Conference on Synthetic Aperture Radar (APSAR), Singapore, 1–4 September 2015; pp. 169–173. [[CrossRef](#)]
51. ESA. *Copernicus Open Access Hub*, 2019. Available online: <https://scihub.copernicus.eu/> (accessed on 28 July 2019).
52. di Bisceglie, M.; Di Santo, M.; Galdi, C.; Lanari, R.; Ranaldo, N. Synthetic Aperture Radar Processing with GPGPU. *IEEE Signal Process. Mag.* **2010**, *27*, 69–78. [[CrossRef](#)]
53. Imperatore, P.; Pepe, A.; Lanari, R. Spaceborne Synthetic Aperture Radar Data Focusing on Multicore-Based Architectures. *IEEE Trans. Geosci. Remote Sens.* **2016**, *54*, 4712–4731. [[CrossRef](#)]
54. Kirk, D.B.; Hwu, W.M.W. *Programming Massively Parallel Processors: A Hands-on Approach*, 1st ed.; Morgan Kaufmann Publishers Inc.: San Francisco, CA, USA, 2010.



© 2019 by the authors. Licensee MDPI, Basel, Switzerland. This article is an open access article distributed under the terms and conditions of the Creative Commons Attribution (CC BY) license (<http://creativecommons.org/licenses/by/4.0/>).